Stability and Transition of the Wake of a Hydrokinetic Axial-Flow Turbine

MARINE 2021

Antonio Posa[1,*] **and Riccardo Broglia**[2]

[1] CNR-INM, Institute of Marine Engineering, National Research Council of Italy, Via di Vallerano 139, 00128, Roma, Italy. E-mail: antonio.posa@inm.cnr.it

[2] CNR-INM, Institute of Marine Engineering, National Research Council of Italy, Via di Vallerano 139, 00128, Roma, Italy. E-mail: riccardo.broglia@cnr.it

[*] Corresponding author: Antonio Posa, antonio.posa@inm.cnr.it

ABSTRACT

A Large-Eddy Simulation study is reported on the wake generated by the rotor of an axial-flow hydrokinetic turbine. The resolution of the computational grid, composed of about 1.9 billion points, enabled us to capture in detail the phenomena of instability of the tip vortices, including long-wave and short-wave instabilities and mutual inductance. We found that these phenomena trigger the process of wake recovery, starting when the coherence of the tip vortices is lost. This allows the free-stream momentum to penetrate into the wake core via both radial inward flows and turbulent mixing.

Keywords: Hydrokinetic energy; Axial-flow turbines; Large-Eddy Simulation; Immersed-Boundary method.

NOMENCLATURE

$A\mathcal{F}$	Radial average of the generic quantity $\mathcal{F}$
C_P	Power coefficient
c_p	Pressure coefficient
C_T	Thrust coefficient
$\mathcal{D}(\cdot)$	Divergence operator
D	Diameter of the turbine
$\boldsymbol{f}$	Forcing term in the momentum equation
$\mathcal{G}(\cdot)$	Gradient operator
k	Turbulent kinetic energy
$\mathcal{L}(\cdot)$	Laplace operator
$\mathcal{L}$	Reference length scale
$\tilde{p}$	Filtered pressure
p_∞	Free-stream pressure
Q	Torque on the rotor
$\mathcal{Q}$	Second-invariant of the velocity gradient tensor
R	Radius of the turbine
r	Radial coordinate in the cylindrical reference frame
Re	Reynolds number
S	Rotor frontal area
T	Thrust on the rotor
t	Time
U_∞	Free-stream velocity

$\tilde{\boldsymbol{u}}$	Filtered velocity vector
u_r	Radial velocity component
u_z	Streamwise velocity component
$\mathcal{V}$	Reference velocity scale
z	Axial coordinate in the cylindrical reference frame
$\bar{\cdot}$	Ensemble-average operator
$\hat{\cdot}$	Phase-average operator
$\tilde{\cdot}$	Filter operator
ν	Kinematic viscosity of the fluid
ρ	Density of the fluid
$\boldsymbol{\tau}$	Subgrid stress tensor
Ω	Rotational speed of the turbine
CEA	French Alternative Energies and Atomic Energy Commission
CFL	Courant-Friedrichs-Lewy number
FT	Flume tank
HPC	High-Performance Computing
IB	Immersed-Boundary
IFREMER	French Research Institute for Exploitation of the Sea
INSEAN	Marine Technology Research Institute
KHL	Kelvin Hydrodynamic Laboratory
KNL	Knights Landing
LES	Large-Eddy Simulation
RANS	Reynolds-averaged Navier-Stokes
SGS	Subgrid stress
TGCC	Très Grand Centre de calcul
TSR	Tip Speed Ratio
TT	Towing tank
WALE	Wall-adaptive local eddy-viscosity

1 INTRODUCTION

Hydrokinetic energy harvesting is expected to provide a significant contribution to meet the growing demand by the world economy and to gradually replace fossil fuels in the next years (see, for instance, the review by Laws and Epps, 2016). Currently, most interest by industry and academia is focused on axial-flow turbines (Kumar and Sarkar, 2016), also thanks to the experience developed over several decades on wind energy. Nonetheless, a full understanding of the process of wake development of the axial-flow turbines has not been achieved yet, in both fields of wind and hydrokinetic energy. In particular, the target of accurately computing the flow downstream of axial-flow turbines is very challenging, because of the complexity of the phenomena of instability of the coherent structures shed by these devices and their long wake development. Properly capturing these features involves a substantial computational effort. Unsteady Reynolds-averaged Navier-Stokes (RANS) approaches are often adopted and well-suited to estimate the performance of an isolated device. However, the accurate solution of the wake signature, which is especially important in defining the influence on the inflow conditions of downstream turbines in farm configurations, requires the use of eddy-resolving methodologies, coupled with numerical methods with optimal conservation properties and very fine computational grids. Therefore, to date only a few computational studies have explored the use of geometry-resolving Large-Eddy Simulation (LES), relying on grids finer than those typically adopted in the framework of RANS computations (Kang *et al.*, 2012; Kang *et al.*, 2014; Chawdhary *et al.*, 2017; Ouro and Stoesser, 2019). Their purpose consists in substantially improving our understanding of the

underlying physics of the wake of axial-flow turbines. This achievement is very much needed. The information provided by high-fidelity simulations in revealing details of the flow physics can be utilized, for instance, to assess the capabilities of turbulence closure strategies adopted by RANS methodologies, to improve their tuning to this particular class of flows and to devise more accurate low-order models of the turbines and their wake, as actuator disks or actuator lines. The simulation of a single turbine using geometry-resolving approaches is indeed already a big challenge, even in a High Performance Computing (HPC) environment. It becomes impossible for farm configurations, even on the most powerful supercomputers in the world. Arrays of turbines are the typical solution for the large-scale harvesting of hydrokinetic energy. Due to computational cost restrictions, the optimization of their layout can only be achieved by means of models (Mycek *et al.*, 2017; Ouro *et al.*, 2019), mimicking in different ways the action of the turbines on the flow or the development of their wake, but needing proper physics-informed tuning via accurate experiments and high-fidelity numerical simulations.

In this work we report LES computations on the rotor of an axial-flow hydrokinetic turbine, conducted on a computational grid consisting of about two billion points. This is an order of magnitude more extensive than in the most advanced studies available today on axial-flow turbines, in both fields of wind and hydrokinetic energy. We verified indeed that the present computations were able to reproduce more in detail the phenomena of instability reported by earlier theoretical works and experimental studies dealing with similar wake systems, as those by Widnall (1972) and Felli *et al.* (2011). In addition, we exploited the large dataset generated by LES to investigate the correlation between the instability of the tip vortices and the mechanism of momentum recovery. As discussed above, the latter is especially important, since it affects the signature of the turbine and the momentum available to downstream devices in farm layouts.

2 METHODOLOGY

The filtered Navier-Stokes equations for incompressible flows were resolved in non-dimensional form:

$$\mathcal{D}(\tilde{\boldsymbol{u}}) \;=\; 0, \tag{1}$$

$$\frac{\partial \tilde{\boldsymbol{u}}}{\partial t} + \mathcal{D}(\tilde{\boldsymbol{u}}\tilde{\boldsymbol{u}}) \;=\; -\mathcal{G}(\tilde{p}) - \mathcal{D}(\boldsymbol{\tau}) + \frac{1}{Re}\mathcal{L}(\tilde{\boldsymbol{u}}) + \boldsymbol{f}, \tag{2}$$

where $\tilde{\boldsymbol{u}}$ and $\tilde{p}$ are the filtered velocity vector and pressure, respectively, $\frac{\partial \tilde{\boldsymbol{u}}}{\partial t}$ is the unsteady term of the momentum equation, $\mathcal{D}(\cdot)$, $\mathcal{G}(\cdot)$ and $\mathcal{L}(\cdot)$ are the divergence, gradient and Laplace operators, Re is the Reynolds number, $\boldsymbol{\tau}$ is the subgrid-scale (SGS) stress tensor and $\boldsymbol{f}$ is a forcing term. The Reynolds number comes from scaling the dimensional Navier-Stokes equations using a reference velocity scale, $\mathcal{V}$, and a reference length scale, $\mathcal{L}$, and is defined as $Re = \mathcal{V}\mathcal{L}/\nu$, where ν stands for the kinematic molecular viscosity of the fluid. The SGS stress tensor, $\boldsymbol{\tau} = \widetilde{\boldsymbol{u}\boldsymbol{u}} - \tilde{\boldsymbol{u}}\tilde{\boldsymbol{u}}$, is the result of filtering the Navier-Stokes equations. It requires to be modeled. In the present study an eddy-viscosity assumption was adopted. In particular, we utilized the Wall-Adapting Local Eddy-viscosity (WALE) model, based on the square of the gradient tensor of the resolved velocity field. Details about this SGS model can be found in Nicoud and Ducros (1999). The forcing term appearing as last quantity in the momentum equation was utilized in the present study to enforce the no-slip boundary condition on the surface of the body "immersed" within the flow, adopting an Immersed-Boundary (IB) methodology. This technique does not require the Eulerian grid, where the Navier-Stokes equations are resolved, to conform the geometry of the body, which is represented by a suitable Lagrangian grid, free to move across the former during the advancement of the solution in time. The boundary conditions are enforced on the surface of the Lagrangian grid by means of a local velocity reconstruction at the points of the Eulerian grid of interface with the Lagrangian grid. This reconstruction is based on the no-slip requirement on the body and the solution of the flow at the fluid points of the Eulerian grid in the vicinity of the interface points. The quantity $\boldsymbol{f}$ is then computed in such a way to enforce that

velocity reconstruction at the interface points of the Eulerian grid. More details on the particular implementation of the IB methodology can be found in Balaras (2004) and Yang and Balaras (2006).

Eqs. 1 and 2 were resolved on a staggered cylindrical grid. Their discretization in space was based on second-order central differences. Their advancement in time was carried out using a fractional-step method (Van Kan, 1986). For the discretization in time of all convective, viscous and SGS terms of radial and axial derivatives the explicit three-step Runge-Kutta scheme was utilized. The implicit Crank-Nicolson scheme was adopted instead for all terms of azimuthal derivatives, to avoid prohibitive stability restrictions on the size of the time step, arising from the strong anisotropy at the axis of the cylindrical grid. The Poisson problem stemming from the continuity condition was resolved using trigonometric transformations along the periodic azimuthal direction, decomposing the original epta-diagonal system of equations into a series of penta-diagonal systems. Then, an efficient direct solver (Rossi and Toivanen, 1999) was utilized to invert each of them. More details on the overall Navier-Stokes solver are reported in Balaras (2004) and Yang and Balaras (2006). Recent applications in the field of renewable energy can be found in Posa (2019), Posa (2020a), Posa (2020b), Posa and Broglia (2021a), Posa and Broglia (2021b).

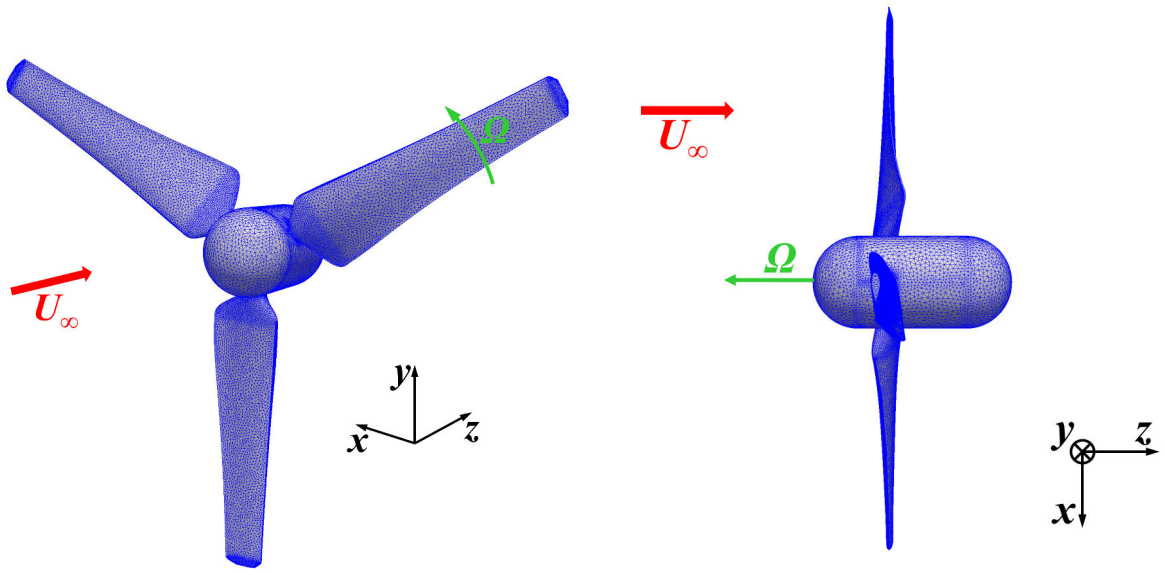

Figure 1. Lagrangian grid representing the simulated geometry.

3 COMPUTATIONAL SETUP

LES was utilized to simulate the rotor of an axial-flow hydrokinetic turbine, composed of three blades. Details on the geometry can be found in the work by Gaurier *et al.* (2015), who reported also experiments on the global performance of the turbine in the framework of a Round Robin study. For the discretization of this geometry we adopted a Lagrangian grid composed of about 75,000 triangles. It is shown in Fig. 1. The filtered Navier-Stokes equations were resolved on a cylindrical grid consisting of about 1.9 billion points. We distributed $900 \times 1026 \times 2050$ points across the radial, azimuthal and axial directions, respectively. Grid spacing was uniform along the azimuthal direction, while stretching was exploited along the radial and axial directions, in order to cluster grid points in the regions of interest, which are that swept by the rotor blades and that of the wake flow. The computational domain extended 2.5 and 7 diameters upstream and downstream of the rotor plane, respectively, while its radial size was of 6 diameters. At the inflow and outflow boundaries uniform free-stream velocity and convective conditions were prescribed, while at the lateral cylindrical boundary a slip wall was utilized to mimic free-stream conditions.

We selected for our simulations values of tip speed ratio and Reynolds number for which measurements were available from the work reported by Gaurier *et al.* (2015). The tip speed ratio is defined as $TSR = \Omega R/U_\infty$, where Ω is the rotational speed of the turbine, R the radius of its rotor and U_∞ the free-stream velocity. In this study it was selected equal to $TSR = 5.0$. The Reynolds number, based on the diameter of the turbine and the free-stream velocity, was equal to $Re = DU_\infty/\nu = 5.6 \times 10^5$.

The computations were carried out enforcing a constant value of $CFL = 1.0$, defining the step of advancement in time based on the instantaneous solution of the flow. This resulted in a very fine resolution in time, equivalent to a rotation of the blades of only 0.076° per time step. Due to the substantial computational effort, this study was performed in a HPC environment, using a parallel solver and dividing the overall flow problem across 2,048 cores of a distributed-memory cluster (Joliot-Curie KNL, TGCC, CEA, France).

Below the results of our computations will be presented both as ensemble-averaged and phase-averaged statistics. The former were computed on the same stationary, cylindrical grid where the filtered Navier-Stokes equations were resolved, while the latter on a cylindrical grid rotating together with the rotor, with the purpose of extracting the coherence of the structures shed from its blades, especially the tip vortices. In the following ensemble- and phase-averaged quantities will be indicated as $\bar{\cdot}$ and $\hat{\cdot}$, respectively. It should be also noted that for simplicity the symbol $\tilde{\cdot}$ for the filter operator will be dropped, assumed that all results reported below will refer to resolved quantities. For the achievement of statistically steady conditions of the wake flow, the solution was developed for two flow-through times, corresponding to about 30 rotations by the turbine. A flow-through time is the time required by the free-stream to cross the whole computational domain. Then, all statistics were computed *on the fly*, considering all instantaneous realizations of the numerical solution, with the purpose of maximizing the size of the statistical sample and minimizing the storage burden. Statistical sampling was carried out during 10 additional rotations. It is also worth noting that in the following discussion all coordinates will be defined in a frame having its origin placed at the intersection between the rotor plane and the axis of the turbine, corresponding to the z-axis, which was oriented along the direction of the free-stream.

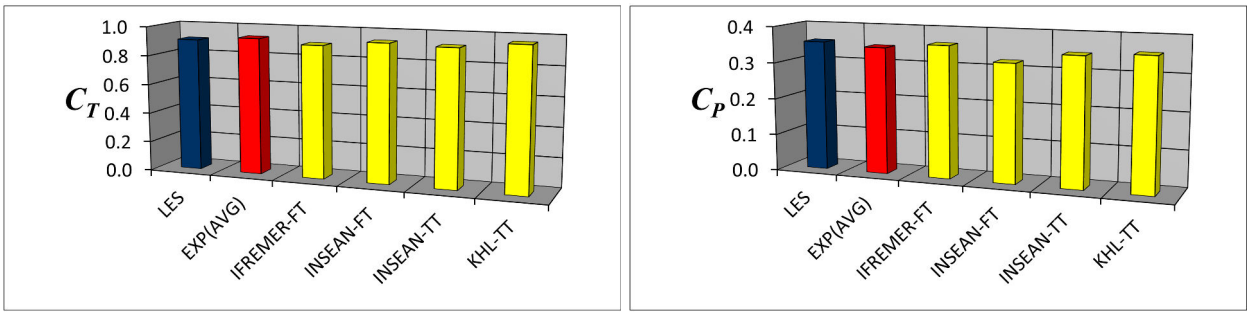

Figure 2. Comparison between present LES computations and measurements by Gaurier *et al.* (2015) on the time-averaged values of thrust and power coefficient in the left and right panels, respectively.

4 COMPARISONS WITH THE EXPERIMENTS

As discussed above, Gaurier *et al.* (2015) conducted measurements on thrust, T, and torque, Q, for a turbine having the same rotor as the one considered in the present study. Therefore, here we report comparisons dealing with the time-averaged values of thrust and power coefficients, defined below:

$$C_T = \frac{T}{\frac{1}{2}\rho S U_\infty^2} \qquad C_P = \frac{Q\Omega}{\frac{1}{2}\rho S U_\infty^3}, \tag{3}$$

where ρ is the density of the fluid (water) and $S = \pi R^2$ is the rotor frontal area.

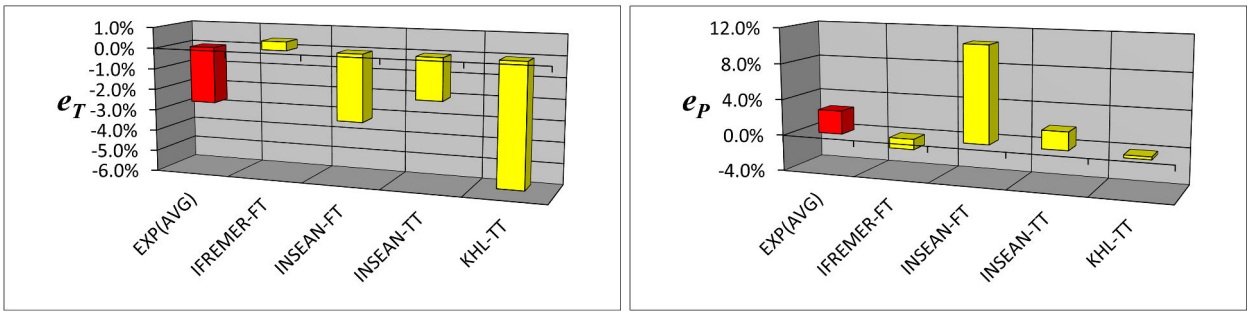

Figure 3. Error of the present LES computations, relative to the measurements by Gaurier *et al.* (2015), on the time-averaged values of thrust and power coefficient in the left and right panels, respectively.

It should be noted that in the present computational study we simulated the rotor geometry only, not including the vertical support required in the experiments by Gaurier *et al.* (2015). In addition, two different hub geometries were considered between experiments and computations. While hub and support do not provide a significant contribution to torque, this is not the case for thrust, since the drag generated by both of them cannot be neglected. However, we were able to overcome this issue, since measurements were available also for the drag coefficient generated by the hub and the support in absence of blades. Therefore, for comparison purposes, we corrected the values of thrust coefficient reported in Gaurier *et al.* (2015), by removing that contribution of drag. In a similar way, the values of C_T and C_P we report here from the present computations take into account the forces and moments acting on the surface of the blades only, excluding the component from the surface of the hub. These results are provided in Fig. 2. Measurements were conducted in the Round Robin campaign by Gaurier *et al.* (2015) at four facilities, two flume tanks (FT) and two towing tanks (TT), respectively. They were carried out at the Kelvin Hydrodynamic Laboratory (KHL) of the Strathclyde University in Glasgow, the French Research Institute for Exploitation of the Sea (IFREMER) at Boulogne sur mer and the Marine Technology Research Institute (INSEAN) in Rome. In Fig. 2 the label EXP(AVG) indicates the average across the four experiments. The agreement of LES with the measurements was found very good, as shown also in Fig. 3, where the error of the computations, relative to each experiment, is reported for both thrust and power coefficients. The error relative to the average across the four experiments is below 3%. Actually, it is biased towards larger values by the dispersion of the measurements, increased especially by those in the towing tank at KHL for the thrust coefficient and those in the flume tank at INSEAN for the power coefficient. In particular, the values for C_T and C_P from LES keep always within the range defined by the experiments.

5 INSTABILITY OF THE TIP VORTICES

The wake shed by the rotor is characterized by strong helical tip vortices, whose instability was found to play a crucial role in the process of wake development and in particular in the mechanism of momentum recovery within the wake core. The tip vortices are illustrated in Fig. 4 by means of instantaneous isosurfaces of pressure coefficient, colored by vorticity magnitude. The pressure coefficient was defined as $c_p = (p - p_\infty)/(0.5\rho U_\infty^2)$, where p_∞ stands for the free-stream pressure. Fig. 4 shows that the tip vortices are very coherent and their helical trajectory very stable within the near wake. However, when they develop instabilities, they start deviating substantially from their helical trajectory, initiating mutual inductance. The latter amplifies the phenomena of instability, leading to very complex trajectories, leapfrogging and eventually to breakdown of the large tip vortices into smaller structures. Fig. 4 shows also that in the region just downstream of the rotor plane the tip vortices experience a shift towards outer radii, corresponding to the expansion of the wake resulting from the deceleration of the flow produced by the turbine. Then, the tip vortices develop downstream across helical trajectories of constant radius, before the development of evident instability phenomena. When the latter occur, the smaller structures originating from the break-up of the tip vortices move

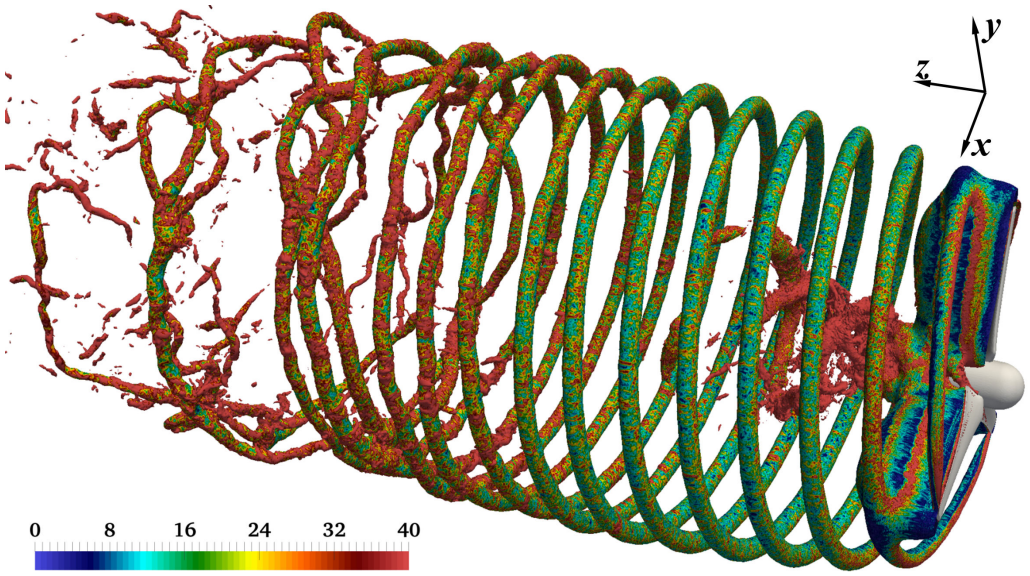

Figure 4. Instantaneous visualization of the tip vortices via isosurfaces of pressure coefficient ($c_p = -0.4$). Colors for the vorticity magnitude, scaled by U_∞/D.

towards inner radii. This phenomenon is illustrated in more detail in the visualization of Fig. 5.

In Fig. 5 the second invariant of the velocity gradient tensor, $\mathcal{Q}$, was utilized to extract the coherence within the wake from an instantaneous realization of the flow. In particular, this quantity was found well-suited to identify the small structures originating from the instability of the large tip vortices. The near wake is dominated by the tip vortices and features a small density of coherent structures, with the exception of its core, which experiences the early instability of the hub vortex, originating a wealth of small structures. However, in the present case the hub vortex was found to play a quite limited role in the process of wake development. As suggested by the visualization in Fig. 4, when the tip vortices experience instability, the smaller structures originating from their break-up start moving towards inner radii. This behavior indicates, as demonstrated later, the onset of the process of wake contraction and recovery. It is triggered by the instability of the tip vortices and promoted by both radial advection and turbulent transport from the free-stream into the wake core.

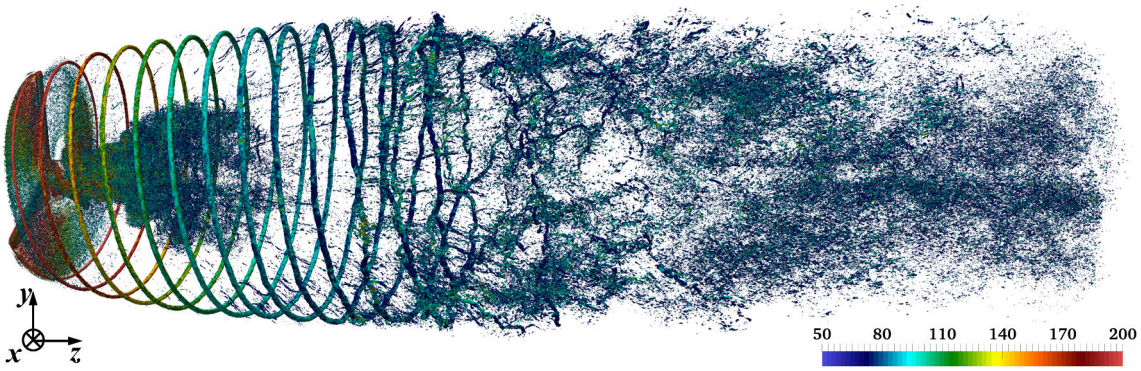

Figure 5. Instantaneous visualization of the tip vortices via isosurfaces of the second invariant of the velocity gradient tensor ($\mathcal{Q}D^2/U_\infty^2 = 1,000$). Colors for the vorticity magnitude, scaled by U_∞/D.

Additional information on the instability of the tip vortices is provided in the detail of Fig. 6. There, a higher value (in magnitude) of the pressure coefficient was considered, compared with Fig. 4, with the purpose of better isolating the core of the tip vortices. As discussed by Widnall (1972), three mechanisms of instability can be identified: short-waves, long-waves and mutual induction. The short- and long-waves instabilities, resulting in deviations from the theoretical helical trajectory, gradually grow as the tip vortices move downstream. We actually verified, reconstructing carefully the development of

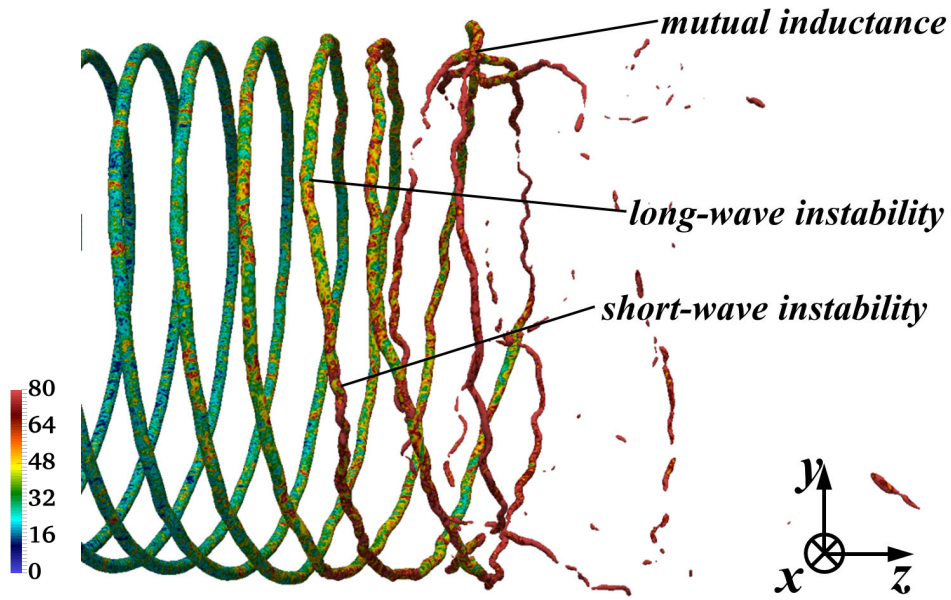

Figure 6. Instantaneous visualization of the tip vortices via isosurfaces of pressure coefficient ($c_p = -0.8$). Detail of the region of instability development and identification of its three major mechanisms: long-waves instabilities, short-waves instabilities and mutual inductance across tip vortices. Colors for the vorticity magnitude, scaled by U_∞/D.

the tip vortices from instantaneous realizations of the solution, that small fluctuations of their trajectory are present since their onset, but these deviations are initially too small to be distinguishable from their visualization. However, Fig. 6 shows that they become soon well distinguishable, leading also to mutual inductance between tip vortices, having the effect of further amplifying the other mechanisms of instability, resulting quickly in the break-up of the tip vortices.

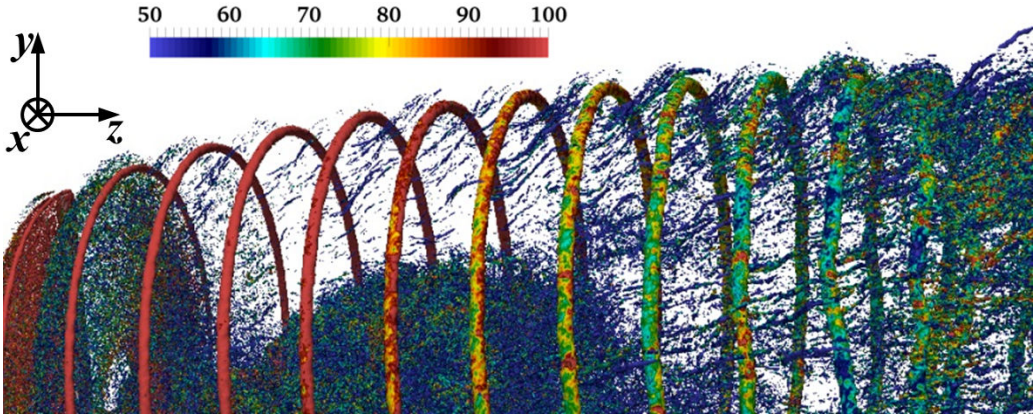

Figure 7. Instantaneous visualization of the tip vortices via isosurfaces of the second invariant of the velocity gradient tensor ($\mathcal{Q}D^2/U_\infty^2 = 500$). Detail of the near wake. Colors for the vorticity magnitude, scaled by U_∞/D.

A detail of Fig. 5, dealing with the near wake of the turbine, is considered in Fig. 7, where actually a smaller value of $\mathcal{Q}$ was selected. It is focused on the small structures, developing at the outer boundary of the wake between neighboring tip vortices. They result from the shear between tip vortices, which was found to play an important role in accelerating the process of instability, as discussed in Posa *et al.* (2021). They become stronger as the wake develops downstream and populate the region where the shear layer shed from the trailing edge of the blades generates a connection between consecutive tip vortices. The latter have indeed a larger pitch, compared to the wake shed by each blade. Therefore, as they move downstream, they come closer to the wake of the preceding blade,

which works as a "bridge" between neighboring tip vortices. The resulting shear promotes turbulence production and contributes to the overall process of instability. A more in depth analysis about this point is reported by Posa *et al.* (2021).

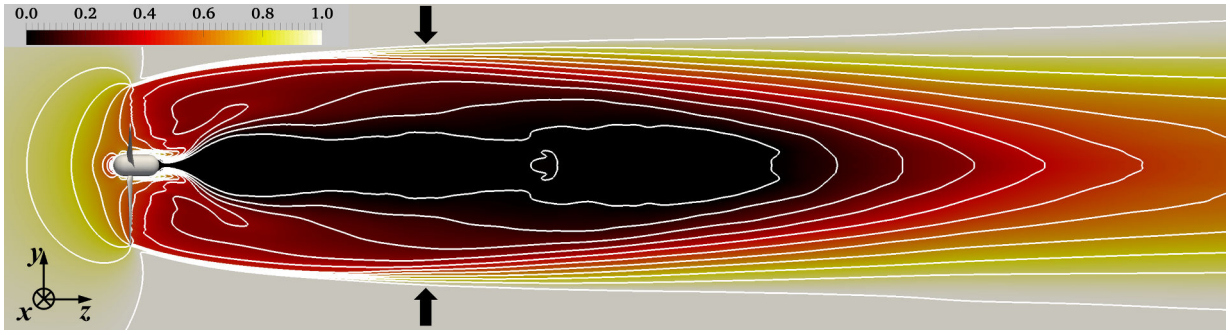

Figure 8. Ensemble-averaged streamwise velocity on a meridian plane through the axis of the turbine. Values scaled by U_∞.

6 WAKE RECOVERY

As discussed above, the instability of the tip vortices starts the process of wake contraction and momentum recovery. As long as the tip vortices keep coherent, they behave as a "shield" at the outer wake boundary, preventing the penetration of higher-momentum fluid from the free-stream into the wake core (Lignarolo *et al.*, 2015). This is shown in Fig. 8, where ensemble-averaged contours of streamwise velocity, $\overline{u}_z$, are reported over a meridian plane through the wake axis. Across the near wake no recovery is observed and the wake boundary experiences a displacement towards outer radii. However, when the instability of the tip vortices develops, the wake boundary moves towards inner radii, as a result of the free-stream momentum beginning to contribute to recovery downstream of the turbine, where the streamwise velocity eventually starts growing. In particular, in Fig. 8 the black arrows indicate the streamwise location at the wake boundary where the radial velocity becomes negative, meaning that the free-stream flow is able to begin the process of momentum replenishment within the wake of the turbine.

The correlation between the instability of the tip vortices, the development of radial inward flows and the process of momentum recovery is illustrated in more detail in Fig. 9. The top panel of Fig. 9 shows ensemble-averaged contours of radial velocity, $\overline{u}_r$. Isolines for the radial velocity are reported in white, with the thickest one corresponding to values of zero velocity, separating the upstream region of wake expansion from the downstream region of wake contraction. Also the isolines for a value of pressure coefficient $\hat{c}_p = -0.3$ are shown in black from the phase-averaged statistics. They allow the identification of the core of the tip vortices, up to the development of instability phenomena. The isolines of pressure coefficient display also the signature of the hub vortex within the wake core, which is actually lost very quickly downstream of the rotor plane, as discussed above. Before instability, the tip vortices are synchronized with the rotation of the turbine, therefore phase-averaging is able to isolate them. After instability, this synchronization is lost and eventually the tip vortices break up into smaller structures, so they cannot be isolated anymore from the phase-averaged statistics of the flow. The top panel of Fig. 9 is very clear in demonstrating that, upstream of the instability of the system of tip vortices the radial velocities at the wake boundary keep positive, the wake is still expanding and the wake core does not start to recover yet, as also shown in Fig. 8. In contrast, when the tip vortices develop instability, the orientation of the radial velocity at outer radii changes: the higher-momentum fluid populating the free-stream starts moving towards the wake core, beginning the process of wake recovery.

Additional evidence of the correlation between the instability of the tip vortices and wake recovery is illustrated in the bottom panel of Fig. 9. There the phase-averaged contours of root-mean-squares

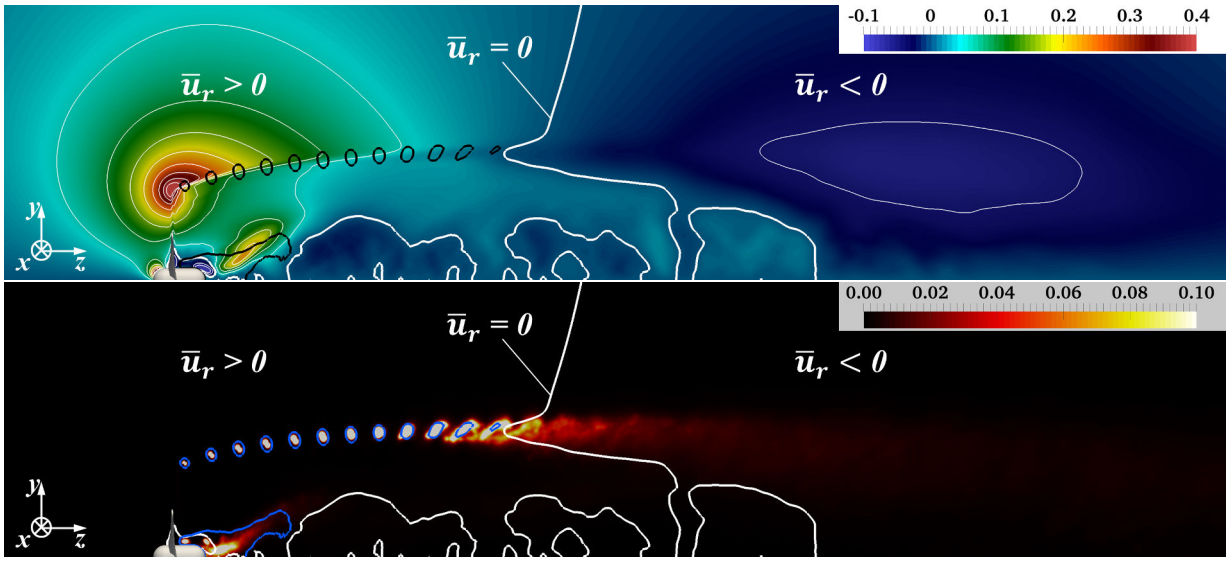

Figure 9. Contours of ensemble-averaged radial velocity (top panel) and phase-averaged root-mean-squares of pressure coefficient (bottom panel) on a meridian plane through the axis of the turbine. In the top panel white and black isolines for the ensemble-averaged radial velocity and for a phase-averaged value of pressure coefficient $\hat{c}_p = -0.3$, respectively. In the bottom panel white and blue isolines for an ensemble-averaged value of radial velocity $\overline{u}_r = 0$ and a phase-averaged value of pressure coefficient $\hat{c}_p = -0.3$, respectively. Radial velocity scaled by U_∞.

of pressure coefficient are reported, again with white isolines of ensemble-averaged radial velocity $\overline{u}_r = 0$ and blue isolines of phase-averaged pressure coefficient $\hat{c}_p = -0.3$. The contours show that the signature of the tip vortices grows in size. This phenomenon is due to their growing instability, resulting in increasing oscillations relative to the mean helical trajectory, smearing the footprint of the vortex core within the phase-averaged statistics of the flow. In addition, it is interesting to notice that, as the wake develops downstream, the areas of large pressure fluctuations become elongated across the direction of shear with the neighboring wake, which is actually the phenomenon already observed above in Fig. 7 by means of the $\mathcal{Q}$-criterion. As demonstrated by the behavior of the radial velocity at the wake boundary, also in the bottom panel of Fig. 9 it is clear that, as long as the tip vortices keep coherent and roughly synchronized with the rotation of the blades, they prevent the free-stream flow from contributing to momentum replenishment at inner radii. Then, when their instability is fully developed the latter process can eventually start.

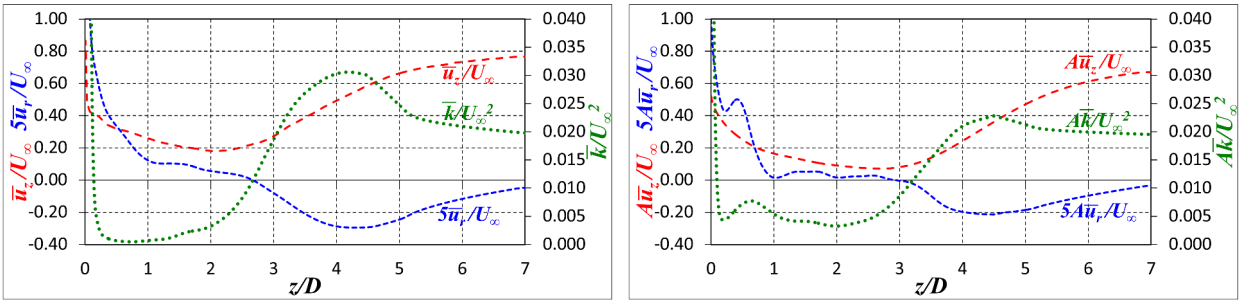

Figure 10. Ensemble-averaged streamwise velocity, radial velocity and turbulent kinetic energy at $r = R$ (left panel) and averaged across the region $0 < r < R$ according to Eq. 4 (right panel).

Fig. 10 shows the streamwise evolution of the ensemble-averaged values of streamwise velocity, radial velocity and turbulent kinetic energy at the boundary of the extraction area and their averages across the extraction area on the left and right panels, respectively. The extraction area is defined at each streamwise coordinate as the projection of the rotor area along the direction of the free-stream. Therefore, the left panel of Fig. 10 shows the ensemble-averaged values at the radial coordinate $r = R$.

In the right panel of Fig. 10 the average of the generic quantity $\mathcal{F}$ (in this case $\overline{u}_z$, $\overline{u}_r$ and $\overline{k}$) was computed as:

$$A\mathcal{F}(z) = \frac{1}{R}\int_{r=0}^{r=R} \mathcal{F}(r,z)dr, \tag{4}$$

where $\mathcal{F}$ is only a function of the radial and streamwise coordinates, since ensemble averages are axisymmetric. In both panels of Fig. 10 the left vertical scale reports the values for the streamwise and radial velocity components, while the right vertical scale those for the turbulent kinetic energy. It should be also noted that, for clarity of visualization, the values of radial velocity were multiplied by a factor 5.

The left panel of Fig. 10 shows that up to 2.5 diameters downstream of the rotor plane the radial velocity at $r = R$ keeps positive. Actually, $\overline{u}_r$ is very large at $z/D = 0$, because of the blockage generated by the rotor. Then, it experiences a sharp decrease. Interestingly, the streamwise velocity starts growing slightly upstream of the inversion of the radial velocity at the wake boundary. For the turbulent kinetic energy this increase is even more evident and already well distinguishable starting at $z/D = 1.0$. The latter is due to the growing instability of the tip vortices. Therefore, turbulent transport is already contributing a mild recovery of streamwise momentum at the wake boundary when the radial velocity is still positive. However, wake recovery becomes much more significant when the full development of the instability of the tip vortices triggers wake contraction and inward radial flows, producing also an additional substantial increase of the levels of turbulent kinetic energy and turbulent mixing between the higher-momentum fluid within the free-stream and the lower-momentum fluid populating the wake. Both turbulent kinetic energy and the negative radial velocity achieve their maxima at about 4 diameters from the rotor plane, which is roughly also the location of the fastest increase of streamwise velocity, thanks to both radial advection and turbulent transport. Further downstream, due to the decline of the radial gradients at $r = R$, both radial flows and turbulence undergo a decrease, resulting into a reduction of the rate of recovery of streamwise velocity.

In the right panel of Fig. 10 similar trends are reported. However, it is possible to notice a delay of the phenomena discussed above with reference to the left panel, since the results visualized in the right panel of Fig. 10 deal with the average across the whole extraction area: turbulent kinetic energy starts growing only at about two diameters downstream of the rotor plane, while up to $z/D \approx 3.0$ the streamwise velocity keeps decreasing and the radial velocity does not switch to negative values. When turbulent mixing and radial advection are already producing a mild momentum recovery at the wake boundary, its core is still not affected. In the present case, the comparison between the left and right panels of Fig. 10 shows that this condition occurs between $2.0 < z/D < 3.0$. Further downstream turbulent transport and radial advection are eventually able to produce a significant momentum replenishment also within the wake core.

7 CONCLUSIONS

A high-fidelity Large-Eddy Simulation on the rotor of an axial-flow hydrokinetic turbine was conducted, using a computational grid at least an order of magnitude finer than in similar studies currently available in the literature. Results were utilized to reveal the role of the tip vortices and their instability in the process of wake recovery. It was verified that, as long as the tip vortices keep coherent, they work as a "shield" to the penetration of the higher free-stream momentum into the wake core. However, when the instability of the system of tip vortices fully develops, a significant momentum replenishment is produced. This is associated with both radial advection and turbulent transport. The former is due to radial inwards flows, the latter to the turbulent mixing phenomena triggered by the destabilization of the tip vortices. The present results are consistent with the behavior observed in earlier experimental studies, where higher levels of free-stream turbulence, accelerating the process of instability of the tip vortices, promoted a faster wake development (Mycek *et al.*, 2014a; Ouro and Stoesser, 2019; Vinod and Banerjee, 2019) and beneficial effects on the performance of downstream turbines in in-line

configurations, thanks to the faster recovery of the wake of the upstream ones (Mycek *et al.*, 2014b; Gaurier *et al.*, 2020; Ebdon *et al.*, 2021).

ACKNOWLEDGEMENTS

We acknowledge PRACE for awarding us access to Joliot Curie KNL at GENCI/CEA, France, with an allocation granted to the project "wakehydroLES – Characterization of the wake of an axial-flow hydrokinetic turbine via LES" (project n. 2019204935) in the framework of the 19^{th} PRACE Call for Proposals for Project Access.

REFERENCES

Balaras, E. (2004). Modeling Complex Boundaries Using an External Force Field on Fixed Cartesian Grids in Large-Eddy Simulations. *Computers & Fluids*, 33(3), 375–404.

Chawdhary, S., Hill, C., Yang, X., Guala, M., Corren, D., Colby, J. and Sotiropoulos, F. (2017). Wake Characteristics of a TriFrame of Axial-Flow Hydrokinetic Turbines. *Renewable Energy*, 109, 332–345.

Ebdon, T., Allmark, M.J., O'Doherty, D.M., Mason-Jones, A., O'Doherty, T., Germain, G. and Gaurier, B. (2021). The Impact of Turbulence and Turbine Operating Condition on the Wakes of Tidal Turbines. *Renewable Energy*, 165, 96–116.

Felli, M., Camussi, R. and Di Felice, F. (2011). Mechanisms of Evolution of the Propeller Wake in the Transition and Far Fields. *Journal of Fluid Mechanics*, 682, 5–53.

Gaurier, B., Germain, G., Facq, J.V., Johnstone, C.M., Grant, A.D., Day, A.H., Nixon, E., Di Felice, F. and Costanzo, M. (2015). Tidal Energy "Round Robin" Tests Comparisons Between Towing Tank and Circulating Tank Results. *International Journal of Marine Energy*, 12, 87–109.

Gaurier, B., Carlier, C., Germain, G., Pinon, G. and Rivoalen, E. (2020). Three Tidal Turbines in Interaction: An Experimental Study of Turbulence Intensity Effects on Wakes and Turbine Performance. *Renewable Energy*, 148, 1150–1164.

Kang, S., Borazjani, I., Colby, J.A. and Sotiropoulos, F. (2012). Numerical Simulation of 3D Flow Past a Real-Life Marine Hydrokinetic Turbine. *Advances in water resources*, 39, 33–43.

Kang, S., Yang, X. and Sotiropoulos, F. (2014). On the Onset of Wake Meandering for an Axial Flow Turbine in a Turbulent Open Channel Flow. *Journal of Fluid Mechanics*, 744, 376–403.

Kumar, D. and Sarkar, S. (2016). A Review on the Technology, Performance, Design Optimization, Reliability, Techno-Economics and Environmental Impacts of Hydrokinetic Energy Conversion Systems. *Renewable and Sustainable Energy Reviews*, 58, 796–813.

Laws, N. and Epps, B. (2016). Hydrokinetic Energy Conversion: Technology, Research, and Outlook. *Renewable and Sustainable Energy Reviews*, 57, 1245–1259.

Lignarolo, L.E.M., Ragni, D., Scarano, F., Simão Ferreira, C. and Van Bussel, G.J.W. (2015). Tip-Vortex Instability and Turbulent Mixing in Wind-Turbine Wakes. *Journal of Fluid Mechanics*, 781, 467–493.

Mycek, P., Gaurier, B., Germain, G., Pinon, G. and Rivoalen, E. (2014a). Experimental Study of the Turbulence Intensity Effects on Marine Current Turbines Behaviour. Part I: One Single Turbine. *Renewable Energy*, 66, 729–746.

Mycek, P., Gaurier, B., Germain, G., Pinon, G. and Rivoalen, E. (2014b). Experimental Study of the Turbulence Intensity Effects on Marine Current Turbines Behaviour. Part II: Two Interacting Turbines. *Renewable Energy*, 68, 876–892.

Mycek, P., Pinon, G., Lothodé, C., Dezotti, A. and Carlier, C. (2017). Iterative Solver Approach for Turbine Interactions: Application to Wind or Marine Current Turbine Farms. *Applied Mathematical Modelling*, 41, 331–349.

Nicoud, F. and Ducros, F. (1999). Subgrid-Scale Stress Modelling Based on the Square of the Velocity Gradient Tensor. *Flow, turbulence and Combustion*, 62(3), 183–200.

Ouro, P., Ramírez, L. and Harrold, M. (2019). Analysis of Array Spacing on Tidal Stream Turbine Farm Performance Using Large-Eddy Simulation. *Journal of Fluids and Structures*, 91, 102732.

Ouro, P. and Stoesser, T. (2019). Impact of Environmental Turbulence on the Performance and Loadings of a Tidal Stream Turbine. *Flow, Turbulence and Combustion*, 102(3), 613–639.

Posa, A. (2019). Wake Characterization of Coupled Configurations of Vertical Axis Wind Turbines Using Large Eddy Simulation. *International Journal of Heat and Fluid Flow*, 75, 27–43.

Posa, A. (2020a). Influence of Tip Speed Ratio on Wake Features of a Vertical Axis Wind Turbine. *Journal of Wind Engineering and Industrial Aerodynamics*, 197, 104076.

Posa, A. (2020b). Dependence of the Wake Recovery Downstream of a Vertical Axis Wind Turbine on Its Dynamic Solidity. *Journal of Wind Engineering and Industrial Aerodynamics*, 202, 104212.

Posa, A. and Broglia, R. (2021a). Characterization of the Turbulent Wake of an Axial-Flow Hydrokinetic Turbine via Large-Eddy Simulation. *Computers & Fluids*, 216, 104815.

Posa, A. and Broglia, R. (2021b). Momentum Recovery Downstream of an Axial-Flow Hydrokinetic Turbine. *Renewable Energy*, 170, 1275–1291.

Posa, A., Broglia, R. and Balaras, E. (2021). Instability of the Tip Vortices Shed by an Axial-Flow Turbine in Uniform Flow. *Submitted to the Journal of Fluid Mechanics*.

Rossi, T. and Toivanen, J. (1999). A Parallel Fast Direct Solver for Block Tridiagonal Systems with Separable Matrices of Arbitrary Dimension. *SIAM Journal on Scientific Computing*, 20(5), 1778–1793.

Van Kan, J.J.I.M. (1986). A Second-Order Accurate Pressure-Correction Scheme for Viscous Incompressible Flow. *SIAM Journal on Scientific and Statistical Computing*, 7(3), 870–891.

Vinod, A. and Banerjee, A. (2019). Performance and Near-Wake Characterization of a Tidal Current Turbine in Elevated Levels of Free Stream Turbulence. *Applied energy*, 254, 113639.

Widnall, S.E. (1972). The Stability of a Helical Vortex Filament. *Journal of Fluid Mechanics*, 54(4), 641–663.

Yang, J. and Balaras, E. (2006). An Embedded-Boundary Formulation for Large-Eddy Simulation of Turbulent Flows Interacting with Moving Boundaries. *Journal of Computational Physics*, 215(1), 12–40.